

Fine-scale electric fields and Joule heating from observations of the Aurora

Patrik Krcelic¹, Patrik Krcelic¹, R C Fear¹, D Whiter¹, B Lanchester¹, A L Aruliah², M Lester³, and L Paxton⁴

¹University of Southampton

²University College London

³University of Leicester

⁴Johns Hopkins University

November 22, 2022

Abstract

Optical measurements from three selected wavelengths have been combined with modelling of emissions from an auroral event to estimate the magnitude and direction of small-scale electric fields on either side of an auroral arc. The temporal resolution of the estimates is 0.1 seconds, which is much higher resolution than measurements from SuperDARN from the same region, with which we compare our estimates. Additionally, we have used the SCANDI instrument to measure the neutral wind during the event in order to calculate the height integrated Joule heating. Joule heating obtained from the small scale electric fields gives larger values (17 {plus minus} 11 and 6 {plus minus} 9 mWm⁻² on average on each side of the arc) than the Joule heating obtained from more conventionally used SuperDARN data (4.8 mWm⁻²). This result indicates that high spatial and temporal resolution electric fields may play an important role in the dynamics of the thermosphere, and thus the ionosphere-magnetosphere system in general.

Hosted file

movie_ap01.gif available at <https://authorea.com/users/535122/articles/598659-fine-scale-electric-fields-and-joule-heating-from-observations-of-the-aurora>

Hosted file

movie_01.gif available at <https://authorea.com/users/535122/articles/598659-fine-scale-electric-fields-and-joule-heating-from-observations-of-the-aurora>

Hosted file

movie_02.gif available at <https://authorea.com/users/535122/articles/598659-fine-scale-electric-fields-and-joule-heating-from-observations-of-the-aurora>

1 **Fine-scale electric fields and Joule heating from**
2 **observations of the Aurora**

3 **P. Krčelić¹, R. C. Fear¹, D. Whiter¹, B. Lanchester¹, A. L. Aruliah², M.**
4 **Lester³, L. Paxton⁴**

5 ¹Physics and Astronomy, University of Southampton, Southampton, UK

6 ²Atmospheric Physics Laboratory, University College London, Gower Street, London, WC1E 6BT, UK

7 ³University of Leicester, Leicester, UK

8 ⁴Applied Physics Laboratory, Johns Hopkins University, Laurel, Maryland, USA

9 **Key Points:**

- 10 • Small scale electric fields are estimated on both sides of an auroral arc using op-
11 tical techniques
- 12 • Joule heating is estimated, by combining optical data with neutral wind obser-
13 vations.
- 14 • Local, high resolution Joule heating shows much higher values than the Joule heat-
15 ing obtained from more averaged radar measurements.

Corresponding author: Patrik Krčelić, P.Krcelic@soton.ac.uk

16 **Abstract**

17 Optical measurements from three selected wavelengths have been combined with
 18 modelling of emissions from an auroral event to estimate the magnitude and direction
 19 of small-scale electric fields on either side of an auroral arc. The temporal resolution of
 20 the estimates is 0.1 seconds, which is much higher resolution than measurements from
 21 SuperDARN from the same region, with which we compare our estimates. Additionally,
 22 we have used the SCANDI instrument to measure the neutral wind during the event in
 23 order to calculate the height integrated Joule heating. Joule heating obtained from the
 24 small scale electric fields gives larger values (17 ± 11 and 6 ± 9 mWm^{-2} on average on
 25 each side of the arc) than the Joule heating obtained from more conventionally used Su-
 26 perDARN data (4.8 mWm^{-2}). This result indicates that high spatial and temporal res-
 27 olution electric fields may play an important role in the dynamics of the thermosphere,
 28 and thus the ionosphere-magnetosphere system in general.

29 **1 Introduction**

30 Magnetosphere-ionosphere interactions play a major role in the dynamics of near
 31 Earth space which also impact the atmosphere and surface infrastructure. Auroral elec-
 32 tric fields are an important link in the magnetosphere-ionosphere interaction, causing
 33 Joule heating in the ionosphere (Lanchester et al., 1996), thus acting as a major source
 34 of high atmosphere dynamics (> 100 km altitude). Ionospheric feedback also occurs,
 35 where the ionosphere plays a significant role in auroral dynamics (Russell et al., 2013).
 36 Measurements of the auroral electric fields have been conducted using rocket and satel-
 37 lite measurements (Marklund et al., 1994), incoherent scatter radar measurements (Lanchester
 38 et al., 1997; Aikio et al., 2002), coherent scatter radars (Chisham et al., 2007), optical
 39 measurements (Tuttle et al., 2014; Dahlgren et al., 2016), or with the combination of two
 40 or more measurement techniques, such as a combination of rocket measurements and ground
 41 auroral imagery (Clayton et al., 2019). The biggest drawback with direct rocket and satel-
 42 lite measurements is the rapid movement of the instrument, resulting in a good spatial
 43 coverage rather than a temporal one. Radar measurements are reliable but have poor
 44 spatial and temporal resolution for small-scale electrodynamics. Measured small scale
 45 electric fields plus measured local neutral wind can be used to estimate Joule heating
 46 (e.g., Billett et al., 2018). Aruliah et al. (2005) investigated JH using 1-min vs 15-min
 47 average European incoherent scatter radar (EISCAT) velocities for a common volume
 48 tristatic FPI-EISCAT experiment, together with the full neutral wind vector obtained
 49 from 3 FabryProt interferometers (FPIs) at Sodankyl, Kiruna and Skibotn. These heat-
 50 ing estimates are usually underestimated and a possible explanation for such underes-
 51 timates could be the highly variable nature of ionospheric electric fields, which is usu-
 52 ally missed with radar observations (Deng & Ridley, 2007). The rapid development of
 53 technology and modelling techniques in the last decades has resulted in more accurate
 54 and more numerous optical studies of the aurora. Dahlgren et al. (2009) first estimated
 55 local drift velocities observing afterglow, using the same optical instrument as used in
 56 this paper, plus modelling techniques. Auroral emission from O^+ (${}^2\text{D}-{}^2\text{P}$) at 732.0 nm
 57 has a lifetime of approximately 5s, and therefore by combining images of this emission
 58 with modelling and images of different prompt emissions, it is possible to determine the
 59 O^+ ion velocity and hence electric field. Tuttle et al. (2020) expanded the technique and
 60 applied it to observations of a single arc structure.

61 In the present paper we have expanded the technique of Tuttle et al. (2020) to es-
 62 timate the small-scale electric fields on either side of an auroral arc. Furthermore, we
 63 have used the measured electric fields to estimate the local height integrated Joule heat-
 64 ing at subsecond resolution.

2 Instruments

2.1 ASK

The Auroral Structure and Kinetics instrument (ASK) is a multimono-chromatic imager designed to measure fine-scale structures of the aurora. ASK consists of 3 cameras observing the magnetic zenith, each with a different narrowband filter centered around a selected wavelength. The cameras are labeled as ASK1, ASK2, and ASK3, and are time synchronised. Each camera uses an electron-multiplying charge-coupled device (EMCCD) detector, with 512 x 512 pixels, binned to 256 x 256 to increase the readout speed. An EMCCD is a photosensitive chip which incorporates electron multiplying in order to amplify weak or single photon events above the read noise (Dahlgren et al., 2016). The optical setting is equipped with f/1 lenses with a focal length of 75 mm, resulting in a $6.2^\circ \times 6.2^\circ$ field of view. Galilean-type converters can be applied to achieve a $3.1^\circ \times 3.1^\circ$ field of view. In the present event the second camera (ASK2) is observing emission from a higher altitude than the other two cameras, so it was equipped with a converter to reduce the field of view, thereby observing the same field lines as ASK1 and ASK3 without converters. During the event studied in this work the instrument was observing at a cadence of 20 Hz.

2.1.1 ASK1 - 673 nm

ASK1 has a filter centered on 673 nm with a passband of 14 nm, observing the N₂ 1PG (first positive group)(5,2) and (4,1) band emissions resulting from the excitation of the N₂ molecules by the precipitating electrons (Ashrafi et al., 2009). The N₂ 1PG emissions show little to no dependence on the energy of the precipitating electrons. N₂ emissions are used to estimate the flux of precipitating electrons by dividing the emission in Rayleighs by a coefficient dependent on the precipitating electron energy distribution for the event, as explained in Lanchester et al. (2009). There are no other emissions contaminating the ASK1 channel.

2.1.2 ASK2 - 732 nm

ASK2 observes emissions from the metastable O⁺(²P) ion with a 1 nm passband centered on 732 nm. Oxygen ions are produced by the electron precipitation. Rees et al. (1982) showed that 18 % of the total O⁺ ionisation results in the O⁺(²P) state, which is further divided into two levels of different total angular momentum: the ²P_{1/2} and ²P_{3/2}. In total we have 4 transitions, (²P_{1/2,3/2} → ²D_{3/2,5/2}), which form 2 doublets (centered on 732 and 733 nm), from which we observe only one doublet with ²D_{5/2} as the lower state. O⁺(²P) states are metastable with a lifetime of ≈ 5 s, which allows the auroral features to be tracked and thus estimate the local electric fields (Dahlgren et al., 2009). Peak emission height of metastable O⁺(²P) ions is around 250 km. The ASK2 channel is contaminated by OH airglow and the (5, 3) band of N₂ 1PG band system. OH airglow decontamination is achieved by background correction, while for the N₂ 1PG decontamination we use the method described in Spry et al. (2014), where we subtract 2.5% of ASK1 image intensity from ASK2 image.

2.1.3 ASK3 - 777 nm

ASK3 observes emissions caused by a transition between the atomic oxygen ⁵P and ⁵S states. The ASK3 filter is centered on 777.4 nm and has a passband of 1.5 nm (Lanchester et al., 2009). The 777.4 nm emissions are highly dependent on the energy of the precipitating electrons. Therefore, the ratio between ASK1 and ASK3 brightness can be used to estimate the precipitating electron energy as described in Lanchester et al. (2009). There are no other emissions contaminating the ASK3 channel.

112

2.2 SuperDARN

113

114

115

116

117

118

119

120

121

122

123

124

125

The Super Dual Auroral Radar Network (SuperDARN) is a network of coherent scatter radars observing the polar cap regions (Chisham et al., 2007). Each radar scans with 16 to 20 beams with each beam scan taking from 3 to 6 seconds, thus resulting in a full radar sweep typically taking 1 or 2 minutes. SuperDARN operates in the high-frequency (HF) range and uses the Doppler shift of radar pulses which are reflected from decametre-scale irregularities in the ionosphere at ≈ 250 km height to obtain the line-of-sight (LOS) ion velocities. In this study, we obtain a 2D horizontal convection velocities from a fitting process which constructs potential maps using all radar measurements in a single radar sweep (Ruohoniemi & Baker, 1998). Note that SuperDARN was not designed to look at the horizontal spatial scales that are being investigated in this study; the purpose of using SuperDARN here is to provide an independent estimate of the convection electric field on the larger scale size that is often used in numerical simulations of the high latitude ionosphere.

126

2.3 SCANDI

127

128

129

130

131

132

133

134

In order to measure the neutral wind velocities we use the Scanning Doppler Imager (SCANDI) located on Svalbard (Aruliah et al., 2010). SCANDI observes an area with 500 km radius over Svalbard, by dividing it into zones in a way which forms multiple concentric rings. LOS neutral wind velocities are measured in each zone using the Doppler shifts of the 630 nm emission from airglow and aurora. The height of peak 630 nm emission, and thus the neutral wind measurements, is 240–250 km. An averaged 2D neutral wind can be obtained from the LOS velocities in each ring of the imaging area. A full sweep of the SCANDI instrument takes around 7.5 minutes.

135

3 Method

136

3.1 Modelling of metastable emissions

137

138

139

140

141

142

143

144

145

146

147

148

149

150

151

152

153

154

155

156

157

158

159

160

The method of Tuttle et al. (2020) has been used in the present work to model the auroral emissions. Full details can be found in that paper, but a brief description is provided here. Prior to the analysis the magnetic zenith needs to be estimated. This is easily done if auroral rays are present in the event. The orientation of the rays and their intersection are then used to give the position of the magnetic zenith. The model is then applied on a 3D grid with dimensions $30 \text{ km} \times 30 \text{ km} \times 410 \text{ km}$. Spatial resolution (both horizontal and vertical) is set to 200 meters and the volume is oriented such that the long axis lies along the magnetic field lines. The process to fill the volume is performed using the following steps. First, the peak energy of precipitating electrons at each pixel is determined using the ratio of the emissions from the images of ASK1 and ASK3 (the two cameras observing prompt emissions). The Southampton ion chemistry model is used (Lanchester et al., 2009), which gives 1D profiles of densities, production and emission of the major species in the Earth’s high altitude atmosphere, with input of the precipitating electron energy distribution, ap and f10.7 indices. A set of profiles is produced by varying the peak energy of the precipitating electron population, but assuming the energy distribution is Gaussian in shape. Each pixel is assigned to a corresponding profile. We then search for the column of a 3D volume where the field of view of a pixel intersects the height of the peak emission from the N_2 1PG profile of a given pixel. The emission profile is then assigned to a given column in a 3D space. This process is done for each pixel in the image in order to fill a 3D volume. For ASK1 and ASK3 the volume is populated with the N_2 1PG and atomic oxygen emissions from the ion chemistry model.

For metastable emissions of ASK2 the volume is filled with the O^+2P production rates since in order to calculate the emissions we need to include the horizontal drift ve-

161 locities in our model. $O^+(2P)$ emission is proportional to the O^+ density distribution
 162 with the continuity equation:

$$163 \quad \frac{dn}{dt} = q - \sum_k \alpha_k n_k n - \sum_j A_j n - \nabla \cdot (n\vec{v}), \quad (1)$$

164
 165 where n is the density of the $O^+(2P)$ ions, q is the production rate of the species,
 166 A_j represent the Einstein coefficients, α represent the quenching rates, n_k are the den-
 167 sities of the quenching species k , and v is a drift velocity. Production rates are obtained
 168 from the ion chemistry model as outlined above (Lanchester et al., 2009). The second
 169 and third terms on the right hand side of the equation are loss processes due to the quench-
 170 ing and the emissions. Particles are quenched in a collisions with other species. There-
 171 fore quenching is greater at regions of increased density (lower altitudes). O^+ is quenched
 172 by the electrons, atomic oxygen and molecular nitrogen. Quenching rates for each species
 173 have been studied in detail (Stephan et al., 2003; Chang et al., 1993; Rees, 1989). The
 174 third term corresponds to the loss due to emission, which is when a particle de-excites
 175 and releases a photon. Einstein emission coefficients are obtained from Zeippen (1987).
 176 The 732 nm emission line has contributions from $J_{1/2}$ and $J_{3/2}$ upper states, which means
 177 we have to solve equation 3.1 twice (once for each state). Since the Southampton ion chem-
 178 istry model gives the production of a whole $O^+(2P)$ ion species, we use the ratio $n_{1/2}/n_{3/2} =$
 179 0.367 given in Whiter et al. (2014) to separate the two states. The continuity equation
 180 is solved using the method described in Gustavsson et al. (2001). Modelled images are
 181 formed from the O^+ density and Einstein coefficients using the blob-based projection
 182 method of Rydester and Gustavsson (2000).

183 The drift velocity in equation 3.1 is treated as a free parameter, which we solve,
 184 by minimising the error:

$$185 \quad err(V) = \sum_{u,v} [I_{obs}(u,v) - I_{mod}(u,v,n(V))]^2. \quad (2)$$

186
 187 $I_{obs}(u,v)$ is the observed intensity at pixel (u,v) , where u and v are coordinates
 188 of the pixel. $I_{mod}(u,v,n(V))$ is the modelled intensity at pixel (u,v) from the camera
 189 field of view for a given O^+ density $n(V)$ which is a function of a free velocity param-
 190 eter V . We are calculating χ^2 values in the same manner, with the assumption that each
 191 pixel (measurement) has the same variance. From χ^2 values we are able to calculate con-
 192 fidence intervals and therefore the standard deviations of free parameters. From the es-
 193 timated drift velocities and the local magnetic field, obtained from IGRF model, the elec-
 194 tric fields are calculated using the following equation:

$$195 \quad \vec{E} = -\vec{v} \times \vec{B} \quad (3)$$

196 where \vec{E} represents the electric field, \vec{B} is the magnetic field and \vec{v} is drift veloc-
 197 ity. We have validated our method by applying it to a synthetically generated auroral
 198 feature with given ion velocities. The details of this method and its results are given in
 199 Appendix 1A..

200 3.2 Double flow

201 The above method assumes that there is only one velocity across the field of view
 202 of the cameras, whereas observations and theory suggest that the electric field is much
 203 more complex in the presence of auroral arcs. The logical next step is therefore to di-
 204 vide the tomographic 3D volume into two parts with different drift velocities. The re-
 205 gion dividing the two volumes is called the separatrix and is defined with two param-

eters, angle θ and distance d from the reference point in a tomographic reference plane. Figure 1 shows a schematic representation of the parameters from the view perpendicular to the magnetic field lines. We are assuming that the drift velocities have a common component (v_{\perp}) across the arc, and different components ($v_{\parallel,1}$, $v_{\parallel,2}$) along the arc. Such a setup has 5 free parameters: θ , d , v_{\perp} , $v_{\parallel,1}$ and $v_{\parallel,2}$. In order to reduce the number of parameters and in turn the computing time, we are determining the separatrix parameters (θ , d) a priori, using the height integrated O⁺2P production rates. From such images we are able to separate the different auroral structures. The separatrix is determined for each time step, and our model is effectively reduced to only 3 free parameters.

3.3 Joule heating estimation

High intensity, short period electric fields obtained from our model are the main contributor to the differences in the local and global heating rates. One of the main goals of the research is to estimate the Joule heating profile, but for that we need the height profiles of both the neutral wind velocity and Pedersen conductivities. Obtaining such profiles is challenging, and therefore we make the following simplifying assumptions. We calculate the height integrated Joule heating ($\sum Q_J$) and the height integrated Pedersen conductivity ($\sum \sigma_P$). It should be noted, that we did not do the height integration but used the empirical formula for height integrated Pedersen conductivity, which assumes integration over the whole column. Electric fields obtained from modelling of the O⁺(²P) ions is assumed to be constant across the height profile due to the assumption of straight, non-diverging magnetic fieldlines in area of observation. We also assume that the average neutral wind (\vec{v}_N) is represented by the neutral wind measurements obtained from the SCANDI instrument. This is a weak assumption since neutral wind changes significantly with height, but as it will be presented in further sections, neutral wind plays a minor role in local, near auroral Joule heating due to the strong and highly variable electric fields. In order to estimate a height integrated Joule heating we use equation (e.g., Billett et al., 2018; Baker et al., 2004):

$$\sum Q_J = \sum \sigma_P E^2 + 2 \sum \sigma_P \vec{E} \cdot (\vec{v}_N \times \vec{B}) + \sum \sigma_P (\vec{v}_N \times \vec{B})^2, \quad (4)$$

where $\sum Q_J$ represents the height integrated Joule heating, $\sum \sigma_P$ height integrated Pedersen conductivity, and \vec{v}_N neutral wind velocity. \vec{E} and \vec{B} are the electric and magnetic fields respectively. The height integrated Pedersen conductivity is estimated using the equations for solar Pedersen conductivity from Rich et al. (1987) and auroral Pedersen conductivity from Robinson et al. (1987). Total Pedersen conductivity is calculated as:

$$\sum \sigma_P = \sqrt{\sum \sigma_{P,A}^2 + \sum \sigma_{P,S}^2}, \quad (5)$$

where $\sum \sigma_{P,A}^2$ and $\sum \sigma_{P,S}^2$ are auroral and solar Pedersen conductivities respectively.

4 Data and Results

For our analysis we are using an event from 21 December, 2014. We have analysed 4 seconds of the increased auroral dynamics centred around the time 22:47:45 UT. During this event IMF B_z was positive and had a value of 3.25 nT, IMF B_y was 10.52 nT and AE index was 444 nT.

Figure 2 shows the Defense Meteorological Satellite Program (DMSP) F16 satellite image of the aurora from observations of Special Sensor Ultraviolet Spectrographic Imager (SSUSI) Lyman-Birge-Hopfield-short (LBH-S) emission. Although the satellite image does not cover Svalbard, the F16 image is the closest available both temporally

251 and spatially to our event. From the location of the auroral zone seen in Fig. 2, and the
 252 fact that we have observed an auroral arc over Svalbard, we can claim with confidence
 253 that Svalbard was at the poleward edge of the auroral zone at the time of our observa-
 254 tion. The SSUSI images show blurred aurora, while the ASK images show a clear and
 255 sharp arc. The reason for this difference lays in both the temporal and spatial resolu-
 256 tions of the two instruments. Since SSUSI images a wider area and samples over a longer
 257 time period, rapidly moving small scale auroral features seem blurred, while ASK can
 258 clearly distinguish such features.

259 Figure 3 shows the time evolution of our event seen from all three ASK cameras.
 260 The black squares on the images for the two prompt emissions (ASK1 and ASK3) rep-
 261 resent the field of view of the ASK2 camera. The time evolution of the metastable emis-
 262 sions during the event can be seen in the second row of figure 3. In the second and third
 263 panels the detachment of two auroral features is marked with arrows. In the fourth panel
 264 the auroral features have reattached into a single arc. The video showing the evolution
 265 of the auroral arc in all three cameras, same as in figure 3 is given in supplementary ma-
 266 terial under the name movie_01.gif.

267 Figure 4 shows the results of the double flow model. The upper row shows the ob-
 268 served metastable emission images, while the bottom row shows the modelled metastable
 269 emission images. Each column matches the four times shown in figure 3. The contours
 270 in the top panels indicate the upper 95 % brightness in the corresponding lower panels.
 271 Comparison of the contours with the background image in the top row shows that the
 272 modelled and observed metastable emissions match well. The video showing the compar-
 273 ison between modelled and observed ASK2 images is given in supplementary material
 274 under the name movie_02.gif.

275 Velocities estimated from the model are shown in figure 5, and the corresponding
 276 electric fields obtained from these velocities are shown in figure 6. Values in figures 5 and
 277 6 represent the magnitudes of the given vectors, while the sign corresponds to the sign
 278 of the x-axis component of each vector. On the north side of the auroral arc, electric fields
 279 are oriented towards the east direction, while on the south side of the auroral arc, the
 280 electric fields are oriented towards the south-east direction. Both sides of the arc show
 281 dynamic behaviour, with a clear shear between them.

282 During the time of the event there were no direct SuperDARN measurements over
 283 Svalbard so we used the fitting technique from Ruohoniemi and Baker (1998) to obtain
 284 a potential map from which we have calculated the background convection velocity. We
 285 have chosen to use an 8th order spherical harmonic fit to the convection pattern, which
 286 provides a better agreement (not shown) between the 'fitted' vectors which result from
 287 the map potential technique, and the 'true' vectors, which combine the measured line
 288 of sight [LOS] velocity components with the components of the fitted vectors that are
 289 transverse to the line of sight direction. Figure 7 shows the potential map with Super-
 290 DARN fitted vectors. The location of Svalbard is indicated by a black rectangle. Although
 291 there is no scatter over Svalbard at this time, we have plotted a "fitted" vector, which
 292 is calculated from the map potential data at the location of the ASK imager, for later
 293 comparison. This is the vector plotted with the larger circle, which lies within the black
 294 box. The estimated velocity of the fitted flow at this point is 412 m/s.

295 The neutral wind velocity obtained from the SCANDI instrument was 169.5 m/s
 296 mostly in the southern direction. Figures 8 and 9 show all velocities in geographic co-
 297 ordinates from the southern and northern sides of the arc, respectively. Blue vectors are
 298 the drift velocities obtained from our model, the red vector is the drift velocity from
 299 SuperDARN, and the black vector is the neutral wind. Figure 8 shows velocities from
 300 the southern side of the arc, while figure 9 shows velocities from the northern side of the
 301 arc. Note, there is a difference in scale on both x and y axes between the two figures.

Table 1. Results of double-flow (marked DF) model, in comparison with the results from SuperDARN. \bar{E} is the average value of electric field, while E_{MAX} is the maximum value in the observed interval. Using the same notation $\overline{\sum Q}$ is the average and $\sum Q_{MAX}$ is the maximum value of height integrated Joule heating. En indicates the energy transferred to the atmosphere during our interval, and is obtained by integrating the Joule heating rate over the 4 s duration of the observations.

	\bar{E} [mVm ⁻¹]	E_{MAX} [mVm ⁻¹]	$\overline{\sum Q}$ [mWm ⁻²]	$\sum Q_{MAX}$ [mWm ⁻²]	En [mJm ⁻²]
DF north	53 ± 15	88 ± 16	17 ± 11	46 ± 18	59 ± 22
DF south	36 ± 17	66 ± 21	6 ± 9	26 ± 19	24 ± 18
SuperDARN	20.2		4.8		17.1

Figure 10 depicts the estimated Joule heating on both sides of the arc using equation (4). The black line in figure 10 represents the height integrated Joule heating using the estimated SuperDARN velocity. Here we can see the differences between Joule heating obtained from local time varying electric fields obtained from our method and Joule heating obtained from more averaged estimated SuperDARN velocity.

Table 1 summarises the results obtained in this paper.

5 Discussion

Small scale electric fields have proven crucial in the estimation of Joule heating in the thermosphere. Using the described method we have obtained the electric fields with temporal resolution of 0.1 seconds and thus have been able to resolve the motion of two auroral features within a single auroral arc. The SuperDARN potential map in Figure 7 indicates complex ionospheric convection during our event. The potential maps were calculated using the full sweep of the SuperDARN radars which took around 1 minute. In the absence of any data over Svalbard, the estimates from SuperDARN are a combination of the effect of the observations to the south and west of Svalbard, and the model potential pattern used for the analysis. As mentioned in Section 2.2, SuperDARN was not designed to make observations on the horizontal spatial scales that are measured by ASK. The purpose of this research is to highlight the importance of the sub-grid physics, which need to be considered in modelling of auroral regions. The electric fields obtained from optical measurements and modelling are from a 4 second interval, in which an auroral arc passed through the ASK camera view. We are treating electric fields from camera measurements as local electric fields related to the auroral dynamics. Our estimated local drift velocities near the auroral arc (0.3-1.5 km/s) are in agreement with the previous study of Tuttle et al. (2020), who estimated drift velocities around an auroral arc to be varying from 0.4 to 1.2 km/s with peak drift velocity of 2.4 km/s, but their estimate represented a spatial average across the entire field of view. Electric fields are highly variable, varying in both direction and intensity. Figure 11 shows drift velocities and electric fields in relation to the auroral arc at 22:47:46.1 UT. The image is from the ASK1 camera (N₂ 1PG emission), and vectors are placed at the center of mass of the traced feature intensity. The black dashed line is the position of the separatrix at 132 km which is the average N₂ 1PG peak emission height for our event. The average electric fields of both features are oriented in the general direction of the arc movement, but in their time evolution electric fields often have different orientation and intensity compared to each other.

336 By further use of the estimated electric fields we are able to estimate the height
 337 integrated Joule heating, while comparing it to a more conventional estimate of the Joule
 338 heating based on SuperDARN data. Our Joule heating estimated from small scale elec-
 339 tric fields has a peak value of 46 ± 18 mW/m² and mean value of 17 ± 11 mW/m² for
 340 the region north of the auroral arc and a peak value of 26 ± 19 mW/m² and mean value
 341 of 6 ± 9 mW/m² for the region south of the auroral arc. The Joule heating estimated
 342 from our optical method shows magnitudes up to 6 times larger on the northern side of
 343 the auroral arc and roughly the same values on the southern side of the auroral arc, com-
 344 pared to ones estimated from lower resolution SuperDARN data. The height integrated
 345 Joule heating obtained from SuperDARN is 4.8 mW/m², which is in agreement with pre-
 346 vious estimates. Baker et al. (2004) used SuperDARN data with the TIMED spacecraft
 347 to obtain heating rates, and estimated peak Joule heating of around 40 mW/m² on the
 348 dusk side of the auroral oval with the values at the edge of the auroral zone close to or
 349 below 10 mW/m². Weimer (2005) used hybrid field aligned currents and electric poten-
 350 tial models to estimate northern hemisphere Joule heating for various geomagnetic condi-
 351 tions. For geomagnetic conditions similar to those in this paper Weimer (2005) obtained
 352 peak auroral zone Joule heating around 7 mW/m² and 4 mW/m² at the poleward edge
 353 of the auroral zone. The highest Joule heating values from Weimer (2005) were obtained
 354 for southward IMF with peak auroral zone Joule heating around 18 mW/m² and 8 mW/m²
 355 at the poleward edge of the auroral zone.

356 The importance of local Joule heating is also highlighted by Kiene et al. (2019) who
 357 combined SuperDARN and Poker Flat Incoherent Scatter Radar (PFISR) to estimate
 358 Joule heating and showed the difference of local hotspots and background Joule heat-
 359 ing to be a factor of 10. In their paper Kiene et al. (2019) have also shown that the Joule
 360 heating is reduced by a factor of 3 with inclusion of neutral wind once it is oriented in
 361 the same direction as the convection velocity. A similar conclusion was given by Billett
 362 et al. (2020), who estimated that the Joule heating is reduced to near zero when the neu-
 363 tral wind has the same orientation as the convection velocity. Our results suggest that
 364 the importance of small scale electric fields is even greater, since the local electric fields
 365 can be more intense and are often in a different direction from the bulk electric field caused
 366 by the convection. Furthermore, because of the highly dynamic nature of the small-scale
 367 electric fields, the neutral wind will not re-orient itself towards the local ion motion but
 368 will stay in the same orientation as the bulk flow, resulting in a high intensity local Joule
 369 heating (although of short duration). Such significant differences between the local and
 370 global estimates indicate the important role of the local Joule heating in the overall dy-
 371 namics of the thermosphere.

372 6 Conclusions

373 Using the ASK instrument and Southampton ion chemistry model we have obtained
 374 small-scale electric fields on each side of an auroral arc for an event at 22:47:45 UT on
 375 21 December 2014. Obtained electric fields have subsecond resolution and peak value
 376 of 88 ± 16 mVm⁻¹ on the northern side of the arc and peak value of 66 ± 21 mVm⁻¹
 377 on the southern side of the arc. Using small scale electric fields and the SCANDI instru-
 378 ment we have calculated the local height integrated Joule heating. Joule heating heat-
 379 ing obtained from small scale electric fields gives much larger values than that obtained
 380 from SuperDARN data. We conclude that with high resolution electric fields we can ob-
 381 tain more accurate (larger) estimates of Joule heating which are usually missed with more
 382 averaged radar measurements. Therefore, small-scale electric fields play a large role in
 383 local, highly intense heating and most likely in overall heating of the ionosphere.

384 Our optical method for estimating electric fields, and consequently the Joule heat-
 385 ing using ASK has proven to be very valuable in understanding the local heating effects
 386 in the vicinity of auroral activity. The method is quite complex, requiring certain con-
 387 ditions to work, such as strong O⁺ (²P) aurora, clear sky and correct estimation of mag-

388 netic zenith. The main goal of further research will be to extend the method to more
 389 complicated cases as well as analysing a wide range of events to reach more general con-
 390 clusions on local Joule heating and its role in large scale dynamics of the upper atmo-
 391 sphere.

392 **Appendix A Ion drift optical method validation using synthetic au-** 393 **roral feature**

394 In order to verify our method we have created a synthetic feature with given ion
 395 drift velocities. We have assumed a simple auroral feature with circular cross-section in
 396 the vertical plane with 2 km diameter and precipitating electron energy of 700 eV. The
 397 flux of precipitating electrons was 6 mWm^{-2} in the innermost 400 m of the feature and
 398 4 mWm^{-2} throughout the rest of the feature. We have made multiple cases of synthetic
 399 spectra. Firstly we have divided our synthetics between those with single frame precip-
 400 itation (a flash-like auroral feature) and those with continuous precipitation throughout
 401 the whole event. Secondly we have added the precipitation source movement which is
 402 seen in our volume as movement with velocity of 2 km/s. The source velocity (both mag-
 403 nitude and direction) was kept constant throughout each individual synthetic event, but
 404 was different for each event. Finally we have added the single ion drifts across the field
 405 of view (single flow case, with x and y components), in a way that the drift velocity in-
 406 creases from 0 to 1.3 km/s with each step and decreases back to zero in a single direc-
 407 tion (eg. x direction). The same drift then occurs in the perpendicular direction (eg. y
 408 direction). We have increased the number of cases by switching the initial direction of
 409 the drift velocity.

410 We have then run our model on synthetic auroral features in order to retrieve the
 411 drift velocities and compare them with those included synthetically. Since all cases gave
 412 similar results we will only present one case. Figure A1 shows the evolution of the syn-
 413 thetic auroral feature in this case, which corresponds to an event for which the precip-
 414 itation was continuous and the source movement changed. Each panel depicts the time
 415 after the start of precipitation shown above each panel. The video showing the evolu-
 416 tion of synthetic auroral feature is given in supplementary material under the name movie_ap01.gif.

417 Figure A2 show the comparison between retrieved drift velocities represented by
 418 the red line and initial drift velocities represented by the black line. The red dashed line
 419 represent the standard deviations of retrieved drift velocities. The upper panel of figure
 420 A2 depicts the x direction of velocities, while the lower panel depicts the y direction. As
 421 seen from both figures, the retrieved velocities match well except for initial 0.5 seconds,
 422 during which time the model corrects and adjusts for the initial conditions. Such behaviour
 423 is seen in all cases, and therefore we have cut the initial 0.5 from all results presented
 424 in this paper.

425 **Acknowledgments**

426 The ASK instrument has been funded by PPARC, STFC and NERC of the UK
 427 and by the Swedish Research Council. The UCL Scanning Doppler Imager (SCANDI)
 428 is maintained thanks to Dr. Ian McWhirter. SuperDARN is funded by national scien-
 429 tific funding agencies of Australia, Canada, China, France, Japan, South Africa, the UK
 430 and the USA. The SuperDARN convection modeling was performed using RST4.1
 431 (<https://github.com/SuperDARN/rst>).

432 PK was supported by NERC INSPIRE studentship NE/S007210/1. RCF was sup-
 433 ported by STFC consolidated grant ST/R000719/1. DKW was supported by NERC In-
 434 dependent Research Fellowship NE/S015167/1. ALA was supported by NERC grants
 435 NE/N004051/1 and NE/W003112/1.

436

References

437

Aikio, A. T., Lakkala, T., Kozlovsky, A., & Williams, P. J. S. (2002). Electric fields and currents of stable drifting auroral arcs in the evening sector. *Journal of Geophysical Research: Space Physics*, *107*(A12), SIA 3-1-SIA 3-14.

439

440

441

442

443

444

445

446

447

Retrieved from <https://agupubs.onlinelibrary.wiley.com/doi/abs/10.1029/2001JA009172> doi: <https://doi.org/10.1029/2001JA009172>

448

449

450

451

452

453

454

455

456

457

458

459

460

461

462

463

464

465

466

467

468

469

470

471

472

473

474

475

476

477

478

479

480

481

482

483

484

485

486

487

488

489

490

Aruliah, A. L., Griffin, E. M., Aylward, A. D., Ford, E. A. K., Kosch, M. J., Davis, C. J., ... Jussila, J. (2005). First direct evidence of meso-scale variability on ion-neutral dynamics using co-located tristatic fpis and eisat radar in northern scandinavia. *Annales Geophysicae*, *23*(1), 147–162. Retrieved from <https://angeo.copernicus.org/articles/23/147/2005/> doi: [10.5194/angeo-23-147-2005](https://doi.org/10.5194/angeo-23-147-2005)

Aruliah, A. L., Griffin, E. M., Yiu, H.-C. I., McWhirter, I., & Charalambous, A. (2010). Scandi-an all-sky doppler imager for studies of thermospheric spatial structure. *Annales Geophysicae*, *28*(2), 549–567. Retrieved from <https://angeo.copernicus.org/articles/28/549/2010/> doi: [10.5194/angeo-28-549-2010](https://doi.org/10.5194/angeo-28-549-2010)

Baker, J. B. H., Zhang, Y., Greenwald, R. A., Paxton, L. J., & Morrison, D. (2004). Height-integrated joule and auroral particle heating in the night side high latitude thermosphere. *Geophysical Research Letters*, *31*(9). Retrieved from <https://agupubs.onlinelibrary.wiley.com/doi/abs/10.1029/2004GL019535> doi: <https://doi.org/10.1029/2004GL019535>

Billett, D. D., Grocott, A., Wild, J. A., Walach, M.-T., & Kosch, M. J. (2018). Diurnal variations in global joule heating morphology and magnitude due to neutral winds. *Journal of Geophysical Research: Space Physics*, *123*(3), 2398–2411. Retrieved from <https://agupubs.onlinelibrary.wiley.com/doi/abs/10.1002/2017JA025141> doi: <https://doi.org/10.1002/2017JA025141>

Billett, D. D., Hosokawa, K., Grocott, A., Wild, J. A., Aruliah, A. L., Ogawa, Y., ... Lester, M. (2020). Multi-instrument observations of ion-neutral coupling in the dayside cusp. *Geophysical Research Letters*, *47*(4), e2019GL085590. Retrieved from <https://agupubs.onlinelibrary.wiley.com/doi/abs/10.1029/2019GL085590> (e2019GL085590 10.1029/2019GL085590) doi: <https://doi.org/10.1029/2019GL085590>

Chang, T., Torr, D. G., Richards, P. G., & Solomon, S. C. (1993). Reevaluation of the $\text{o}^+(\text{p})$ reaction rate coefficients derived from atmosphere explorer c observations. *Journal of Geophysical Research: Space Physics*, *98*(A9), 15589–15597. Retrieved from <https://agupubs.onlinelibrary.wiley.com/doi/abs/10.1029/93JA00957> doi: <https://doi.org/10.1029/93JA00957>

Chisham, G., Lester, M., Milan, S., Freeman, M., Bristow, W., Grocott, A., ... others (2007). A decade of the super dual auroral radar network (superdarn): Scientific achievements, new techniques and future directions. *Surveys in geophysics*, *28*(1), 33–109.

Clayton, R., Lynch, K., Zettergren, M., Burleigh, M., Conde, M., Grubbs, G., ... Varney, R. (2019). Two-dimensional maps of in situ ionospheric plasma flow data near auroral arcs using auroral imagery. *Journal of Geophysical Research: Space Physics*, *124*(4), 3036–3056. Retrieved from <https://agupubs.onlinelibrary.wiley.com/doi/abs/10.1029/2018JA026440> doi: <https://doi.org/10.1029/2018JA026440>

Dahlgren, H., Ivchenko, N., Lanchester, B., Ashrafi, M., Whiter, D., Marklund, G., & Sullivan, J. (2009). First direct optical observations of plasma flows using afterglow of o^+ in discrete aurora. *Journal of Atmospheric and Solar-Terrestrial Physics*, *71*(2), 228–238. Retrieved from <https://www.sciencedirect.com/science/article/pii/S1364682608003751> doi: <https://doi.org/10.1016/j.jastp.2008.11.015>

Dahlgren, H., Lanchester, B. S., Ivchenko, N., & Whiter, D. K. (2016). Electro-

- 491 dynamics and energy characteristics of aurora at high resolution by optical
 492 methods. *Journal of Geophysical Research: Space Physics*, 121(6), 5966-5974.
 493 Retrieved from [https://agupubs.onlinelibrary.wiley.com/doi/abs/](https://agupubs.onlinelibrary.wiley.com/doi/abs/10.1002/2016JA022446)
 494 [10.1002/2016JA022446](https://doi.org/10.1002/2016JA022446) doi: <https://doi.org/10.1002/2016JA022446>
- 495 Deng, Y., & Ridley, A. J. (2007). Possible reasons for underestimating joule heating
 496 in global models: E field variability, spatial resolution, and vertical veloc-
 497 ity. *Journal of Geophysical Research: Space Physics*, 112(A9). Retrieved
 498 from [https://agupubs.onlinelibrary.wiley.com/doi/abs/10.1029/](https://agupubs.onlinelibrary.wiley.com/doi/abs/10.1029/2006JA012006)
 499 [2006JA012006](https://doi.org/10.1029/2006JA012006) doi: <https://doi.org/10.1029/2006JA012006>
- 500 Gustavsson, B., Sergienko, T., Rietveld, M. T., Honary, F., Steen, A., Brndstrm,
 501 B. U. E., ... Marple, S. (2001). First tomographic estimate of volume dis-
 502 tribution of hf-pump enhanced airglow emission. *Journal of Geophysical*
 503 *Research: Space Physics*, 106(A12), 29105-29123. Retrieved from [https://](https://agupubs.onlinelibrary.wiley.com/doi/abs/10.1029/2000JA900167)
 504 [agupubs.onlinelibrary.wiley.com/doi/abs/10.1029/2000JA900167](https://doi.org/10.1029/2000JA900167) doi:
 505 <https://doi.org/10.1029/2000JA900167>
- 506 Kiene, A., Bristow, W. A., Conde, M. G., & Hampton, D. L. (2019). High-
 507 resolution local measurements of f region ion temperatures and joule heat-
 508 ing rates using superdarn and ground-based optics. *Journal of Geophys-*
 509 *ical Research: Space Physics*, 124(1), 557-572. Retrieved from [https://](https://agupubs.onlinelibrary.wiley.com/doi/abs/10.1029/2018JA025997)
 510 [agupubs.onlinelibrary.wiley.com/doi/abs/10.1029/2018JA025997](https://doi.org/10.1029/2018JA025997) doi:
 511 <https://doi.org/10.1029/2018JA025997>
- 512 Lanchester, B. S., Ashrafi, M., & Ivchenko, N. (2009). Simultaneous imaging
 513 of aurora on small scale in oi (777.4 nm) and n₂1p to estimate energy and
 514 flux of precipitation. *Annales Geophysicae*, 27(7), 2881-2891. Retrieved
 515 from <https://angeo.copernicus.org/articles/27/2881/2009/> doi:
 516 [10.5194/angeo-27-2881-2009](https://doi.org/10.5194/angeo-27-2881-2009)
- 517 Lanchester, B. S., Kaila, K., & McCrea, I. W. (1996). Relationship between large
 518 horizontal electric fields and auroral arc elements. *Journal of Geophysical Re-*
 519 *search: Space Physics*, 101(A3), 5075-5084. Retrieved from [https://agupubs](https://agupubs.onlinelibrary.wiley.com/doi/abs/10.1029/95JA02055)
 520 [.onlinelibrary.wiley.com/doi/abs/10.1029/95JA02055](https://doi.org/10.1029/95JA02055) doi: [https://doi](https://doi.org/10.1029/95JA02055)
 521 [.org/10.1029/95JA02055](https://doi.org/10.1029/95JA02055)
- 522 Lanchester, B. S., Rees, M. H., Lummerzheim, D., Otto, A., Frey, H. U., & Kaila,
 523 K. U. (1997). Large fluxes of auroral electrons in filaments of 100 m width.
 524 *Journal of Geophysical Research: Space Physics*, 102(A5), 9741-9748. Re-
 525 trieved from [https://agupubs.onlinelibrary.wiley.com/doi/abs/](https://agupubs.onlinelibrary.wiley.com/doi/abs/10.1029/97JA00231)
 526 [10.1029/97JA00231](https://doi.org/10.1029/97JA00231) doi: <https://doi.org/10.1029/97JA00231>
- 527 Marklund, G., Blomberg, L., Flthammar, C.-G., & Lindqvist, P.-A. (1994).
 528 On intense diverging electric fields associated with black aurora. *Geo-*
 529 *physical Research Letters*, 21(17), 1859-1862. Retrieved from [https://](https://agupubs.onlinelibrary.wiley.com/doi/abs/10.1029/94GL00194)
 530 [agupubs.onlinelibrary.wiley.com/doi/abs/10.1029/94GL00194](https://doi.org/10.1029/94GL00194) doi:
 531 <https://doi.org/10.1029/94GL00194>
- 532 Rees, M. H. (1989). *Physics and chemistry of the upper atmosphere*. Cambridge Uni-
 533 versity Press.
- 534 Rees, M. H., Abreu, V. J., & Hays, P. B. (1982). The production efficiency of
 535 o+(p) ions by auroral electron impact ionization. *Journal of Geophysical*
 536 *Research: Space Physics*, 87(A5), 3612-3616. Retrieved from [https://](https://agupubs.onlinelibrary.wiley.com/doi/abs/10.1029/JA087iA05p03612)
 537 [agupubs.onlinelibrary.wiley.com/doi/abs/10.1029/JA087iA05p03612](https://doi.org/10.1029/JA087iA05p03612)
 538 doi: <https://doi.org/10.1029/JA087iA05p03612>
- 539 Rich, F. J., Gussenhoven, M. S., & Greenspan, M. E. (1987, December). Using
 540 simultaneous particle and field observations on a low altitude satellite to es-
 541 timate Joule heat energy flow into the high latitude ionosphere. *Annales*
 542 *Geophysicae*, 5, 527-534.
- 543 Robinson, R. M., Vondrak, R. R., Miller, K., Dabbs, T., & Hardy, D. (1987). On
 544 calculating ionospheric conductances from the flux and energy of precipitating
 545 electrons. *Journal of Geophysical Research: Space Physics*, 92(A3), 2565-

2569. Retrieved from <https://agupubs.onlinelibrary.wiley.com/doi/abs/10.1029/JA092iA03p02565> doi: <https://doi.org/10.1029/JA092iA03p02565>
- 548 Ruohoniemi, J. M., & Baker, K. B. (1998). Large-scale imaging of high-latitude con-
549 vection with super dual auroral radar network hf radar observations. *Journal*
550 *of Geophysical Research: Space Physics*, *103*(A9), 20797-20811. Retrieved from
551 <https://agupubs.onlinelibrary.wiley.com/doi/abs/10.1029/98JA01288>
552 doi: <https://doi.org/10.1029/98JA01288>
- 553 Russell, A. J. B., Wright, A. N., & Streltsov, A. V. (2013). Production of
554 small-scale alfvén waves by ionospheric depletion, nonlinear magnetosphere-
555 ionosphere coupling and phase mixing. *Journal of Geophysical Re-*
556 *search: Space Physics*, *118*(4), 1450-1460. Retrieved from [https://](https://agupubs.onlinelibrary.wiley.com/doi/abs/10.1002/jgra.50168)
557 agupubs.onlinelibrary.wiley.com/doi/abs/10.1002/jgra.50168 doi:
558 <https://doi.org/10.1002/jgra.50168>
- 559 Rydester, P., & Gustavsson, B. (2000). Investigation of smooth basis functions
560 and an approximated projection algorithm for faster tomography. *Interna-*
561 *tional Journal of Imaging Systems and Technology*, *11*(6), 347-354. Retrieved
562 from <https://onlinelibrary.wiley.com/doi/abs/10.1002/ima.1019> doi:
563 <https://doi.org/10.1002/ima.1019>
- 564 Spry, J., Jokiahho, O., Lanchester, B., & Whiter, D. (2014). Modelling n21p contam-
565 ination in auroral o+ emissions. *Journal of Atmospheric and Solar-Terrestrial*
566 *Physics*, *107*, 8-11. Retrieved from [https://www.sciencedirect.com/](https://www.sciencedirect.com/science/article/pii/S1364682613002848)
567 [science/article/pii/S1364682613002848](https://www.sciencedirect.com/science/article/pii/S1364682613002848) doi: [https://doi.org/10.1016/](https://doi.org/10.1016/j.jastp.2013.10.013)
568 [j.jastp.2013.10.013](https://doi.org/10.1016/j.jastp.2013.10.013)
- 569 Stephan, A. W., Meier, R. R., Dymond, K. F., Budzien, S. A., & McCoy, R. P.
570 (2003). Quenching rate coefficients for o+(2p) derived from middle ultra-
571 violet airglow. *Journal of Geophysical Research: Space Physics*, *108*(A1).
572 Retrieved from [https://agupubs.onlinelibrary.wiley.com/doi/abs/](https://agupubs.onlinelibrary.wiley.com/doi/abs/10.1029/2002JA009540)
573 [10.1029/2002JA009540](https://agupubs.onlinelibrary.wiley.com/doi/abs/10.1029/2002JA009540) doi: <https://doi.org/10.1029/2002JA009540>
- 574 Tuttle, S., Gustavsson, B., & Lanchester, B. (2014). Temporal and spatial evolu-
575 tion of auroral electron energy spectra in a region surrounding the magnetic
576 zenith. *Journal of Geophysical Research: Space Physics*, *119*(3), 2318-2327.
577 Retrieved from [https://agupubs.onlinelibrary.wiley.com/doi/abs/](https://agupubs.onlinelibrary.wiley.com/doi/abs/10.1002/2013JA019627)
578 [10.1002/2013JA019627](https://agupubs.onlinelibrary.wiley.com/doi/abs/10.1002/2013JA019627) doi: <https://doi.org/10.1002/2013JA019627>
- 579 Tuttle, S., Lanchester, B., Gustavsson, B., Whiter, D., Ivchenko, N., Fear, R., &
580 Lester, M. (2020). Horizontal electric fields from flow of auroral o+(2p) ions
581 at sub-second temporal resolution. *Annales Geophysicae*, *38*(4), 845-859. Re-
582 trieved from <https://angeo.copernicus.org/articles/38/845/2020/> doi:
583 [10.5194/angeo-38-845-2020](https://doi.org/10.5194/angeo-38-845-2020)
- 584 Weimer, D. R. (2005). Improved ionospheric electrodynamic models and appli-
585 cation to calculating joule heating rates. *Journal of Geophysical Research:*
586 *Space Physics*, *110*(A5). Retrieved from [https://agupubs.onlinelibrary](https://agupubs.onlinelibrary.wiley.com/doi/abs/10.1029/2004JA010884)
587 [.wiley.com/doi/abs/10.1029/2004JA010884](https://agupubs.onlinelibrary.wiley.com/doi/abs/10.1029/2004JA010884) doi: [https://doi.org/10.1029/](https://doi.org/10.1029/2004JA010884)
588 [2004JA010884](https://doi.org/10.1029/2004JA010884)
- 589 Whiter, D. K., Lanchester, B. S., Gustavsson, B., Jallo, N. I. B., Jokiahho, O.,
590 Ivchenko, N., & Dahlgren, H. (2014, nov). Relative brightness of the o+(2d-
591 2p) doublets in low-energy aurorae. *The Astrophysical Journal*, *797*(1), 64.
592 Retrieved from <https://doi.org/10.1088/0004-637x/797/1/64> doi:
593 [10.1088/0004-637x/797/1/64](https://doi.org/10.1088/0004-637x/797/1/64)
- 594 Zeippen, C. (1987). Improved radiative transition probabilities for o ii forbidden
595 lines. *Astronomy and Astrophysics*, *173*, 410-414.

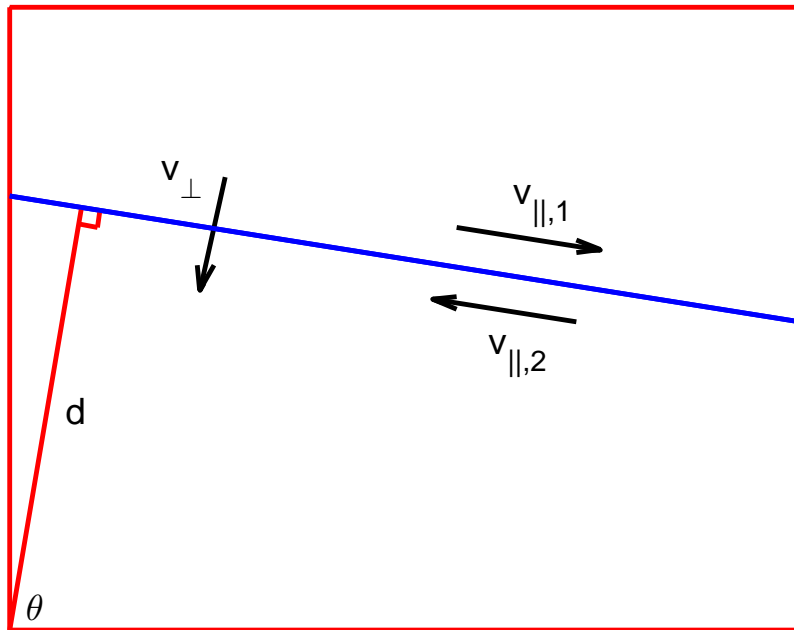


Figure 1. Schematic representation of model parameters, from top view of tomographic volume. The blue line represents the separatrix, while black vectors represent velocities. θ , d are separatrix parameters and, v_{\perp} , $v_{\parallel,1}$, $v_{\parallel,2}$ are given velocities.

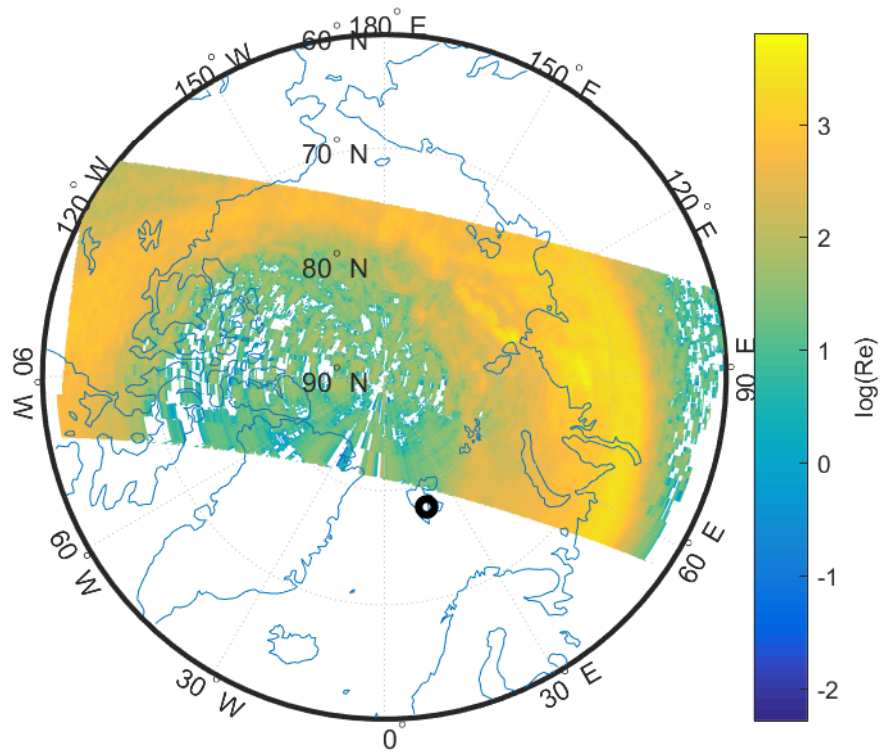


Figure 2. Auroral LBH-S emission seen from DMSP F16 spacecraft cut in time between 23:15:18 and 23:31:25 UT on 21 December 2014. Results are given in geographical coordinates and the location of Svalbard is indicated with a black circle.

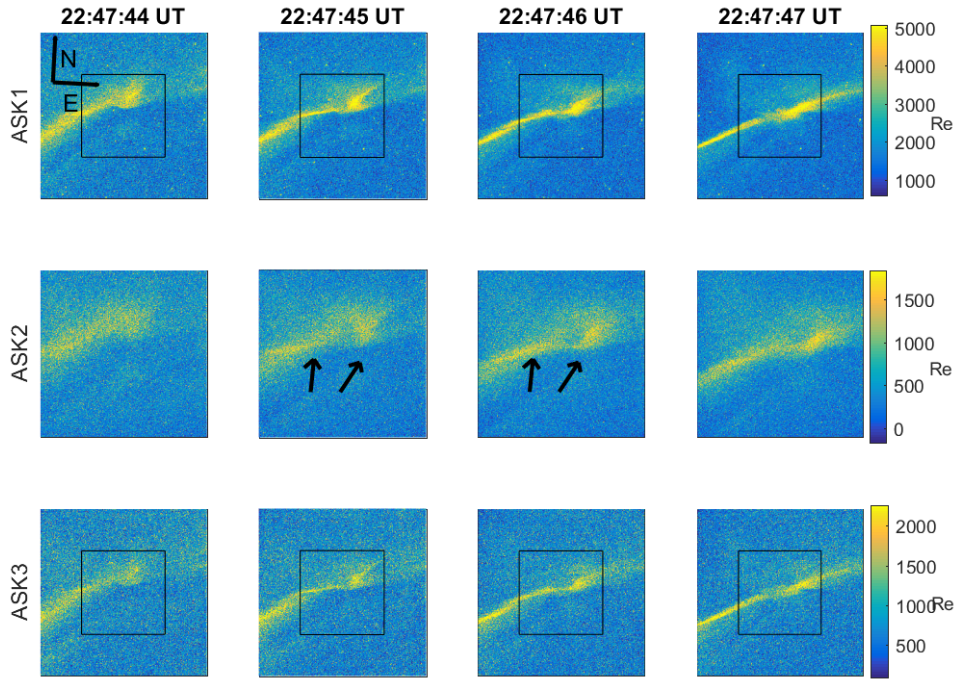


Figure 3. Evolution of the auroral features on 21 December, 2014, as seen from the three ASK cameras. Rows indicate the ASK camera number, while columns indicate the times of images labeled above. ASK1 and ASK3 are cameras observing two prompt emissions. ASK2 is the camera observing metastable emission. During this event a telescope was present on ASK2 so the black rectangles on the ASK1 and ASK3 images represent the field of view of ASK2.

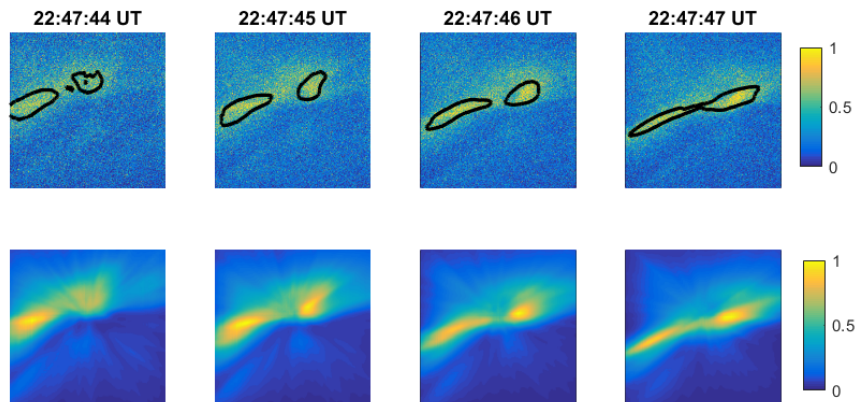


Figure 4. Comparison between modelled and observed images of metastable O^+ . Top row shows observed and bottom row modelled images. Contours on the observed images represent the 95% level of the modelled brightness. Time in UT is indicated on top of each column.

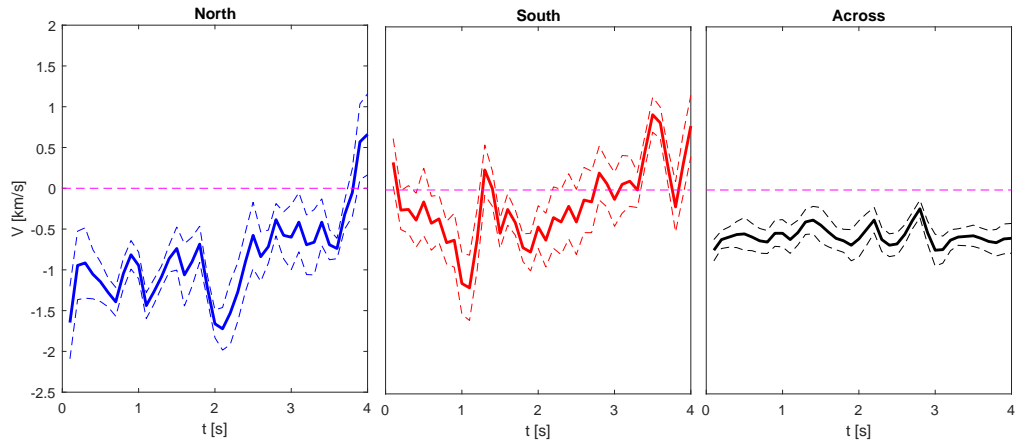


Figure 5. Modelled velocities for each time step. The blue line represents northern parallel velocity, the red line represents southern parallel velocity and the black line represents velocity across the arc. Dashed lines represent standard deviations.

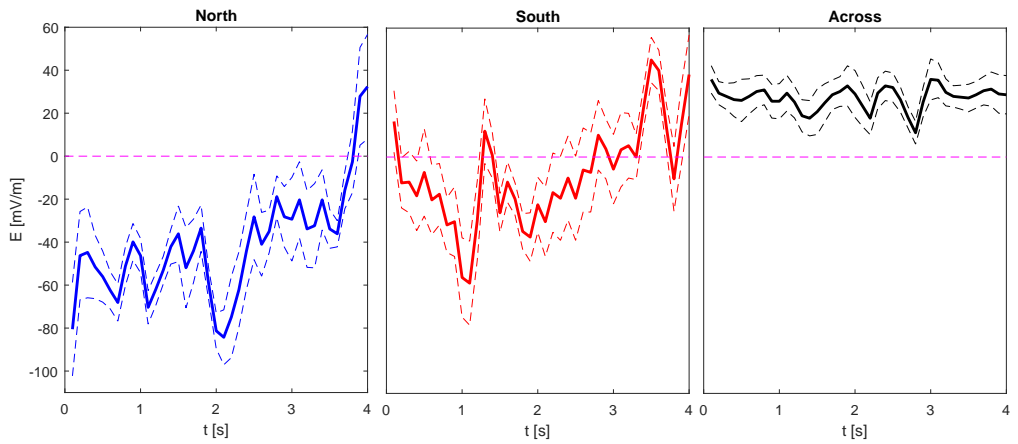


Figure 6. Modelled electric fields for each time step. Line colours are the same as in figure 5.

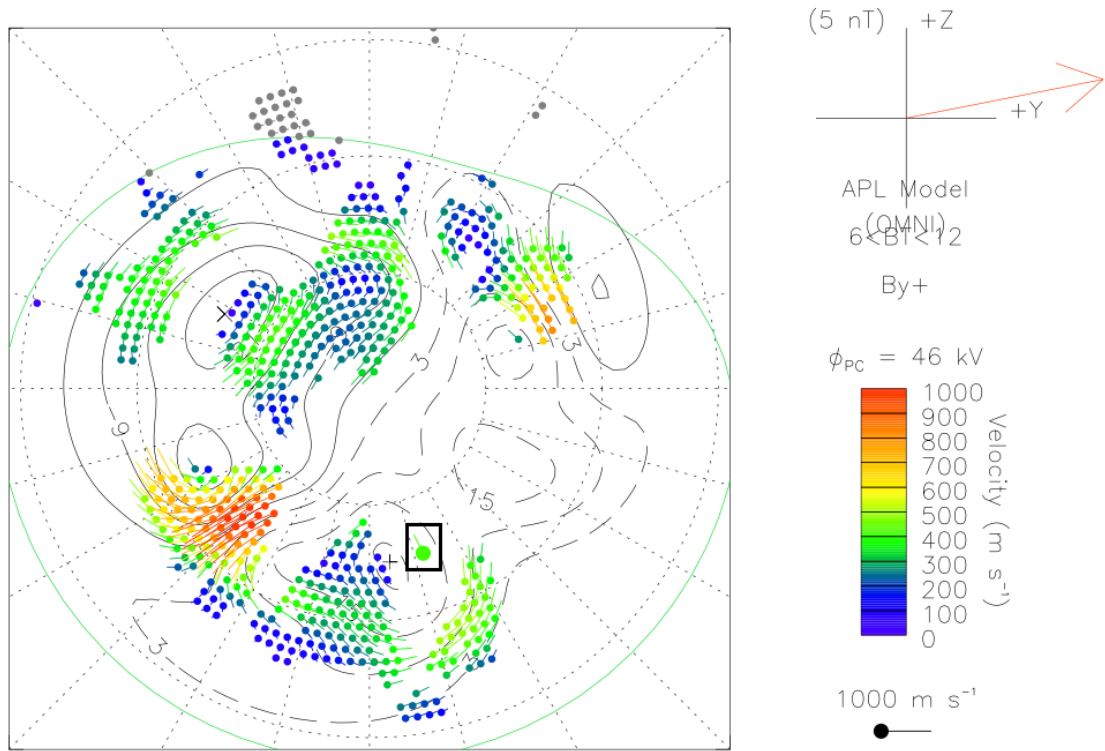


Figure 7. The SuperDARN fitted vectors and contours. The Svalbard location is indicated with a black rectangle.

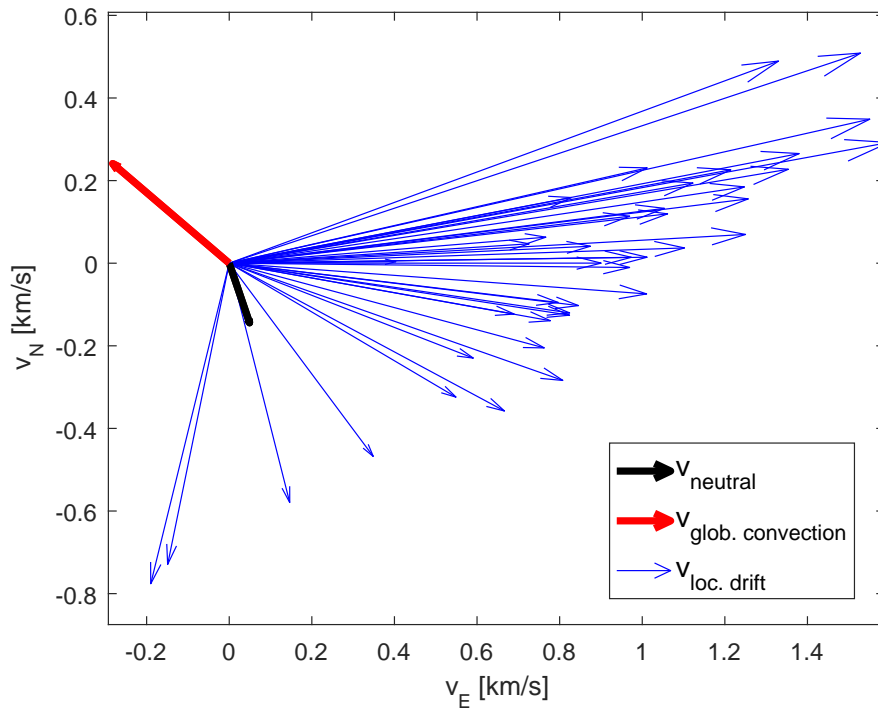


Figure 8. Velocities in the area north of the auroral arc shown in geographic system. Blue vectors represent the drift velocities from optical measurements north of the auroral arc, the red vector represents convection from SuperDARN and the black vector represents the neutral wind obtained from SCANDI.

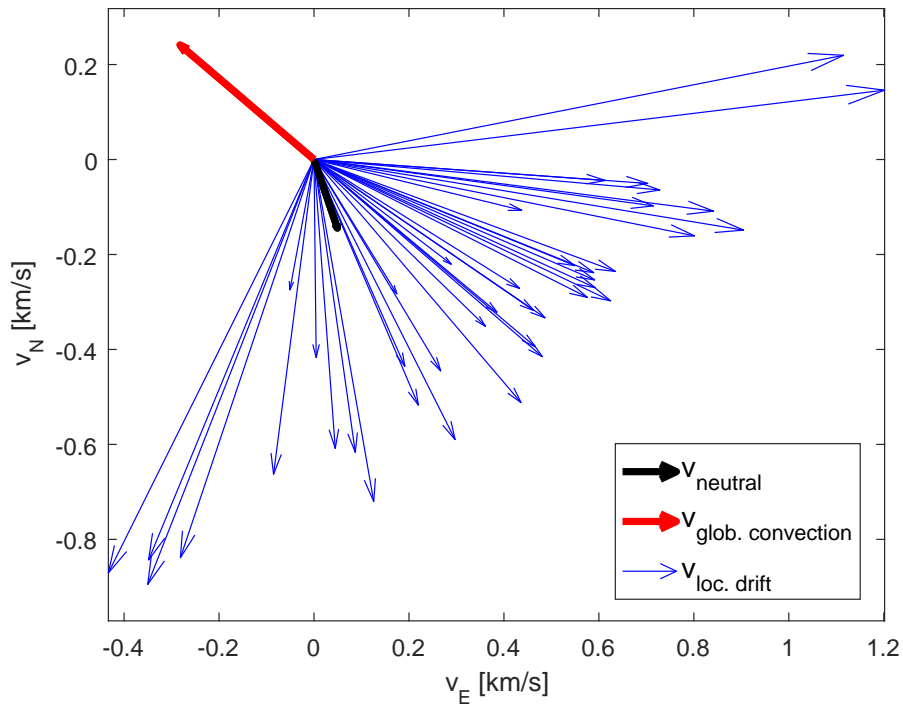


Figure 9. Velocities in the area south of the auroral arc shown in geographic system. Blue vectors represents drift velocities from optical measurements south of the arc. The rest of the vectors are the same as in figure 8.

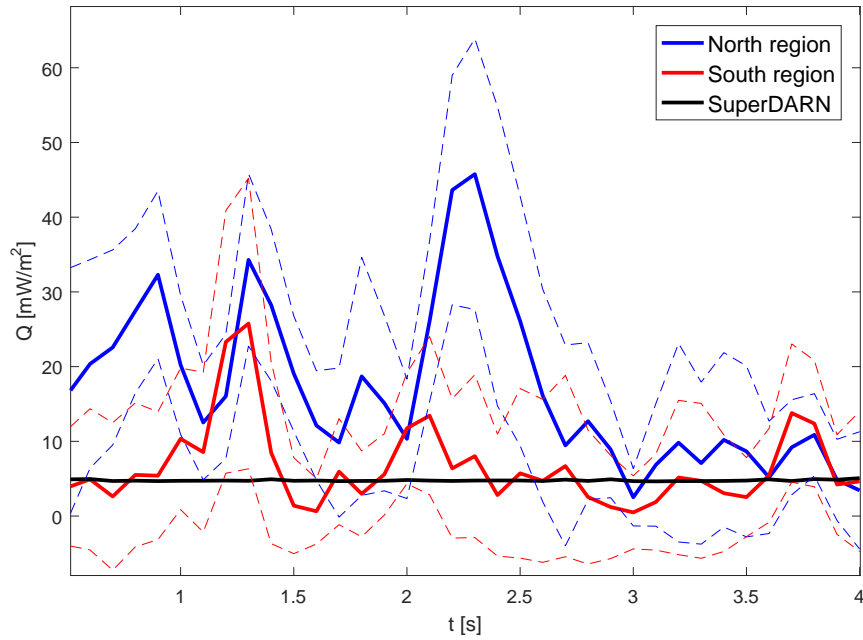


Figure 10. Height integrated Joule heating from both sides of the arc compared with SuperDARN estimates. The red line represents Joule heating south of the auroral arc, the blue line represents Joule heating north of the auroral arc and the black line represents Joule heating obtained from SuperDARN measurements.

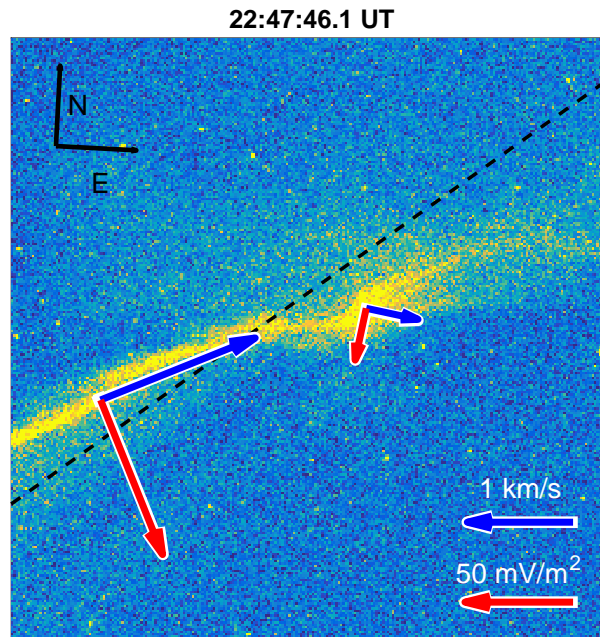


Figure 11. Estimated drifts and electric fields in relation with observed auroral arc. The blue vectors represent drift velocities, the red vectors represent electric field, and black dashed line represent separatrix at 132 km altitude. Vector scales are given in the lower right corner of the panel.

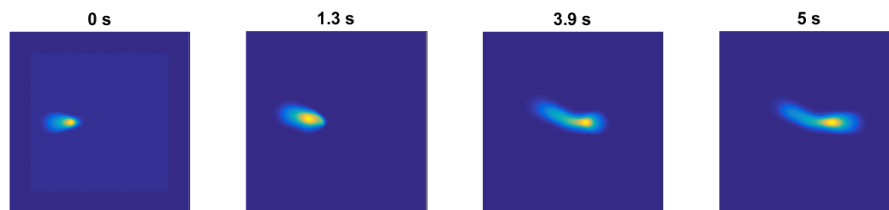


Figure A1. Evolution of synthetic auroral feature. Each panel depicts different timesteps labeled above each panel.

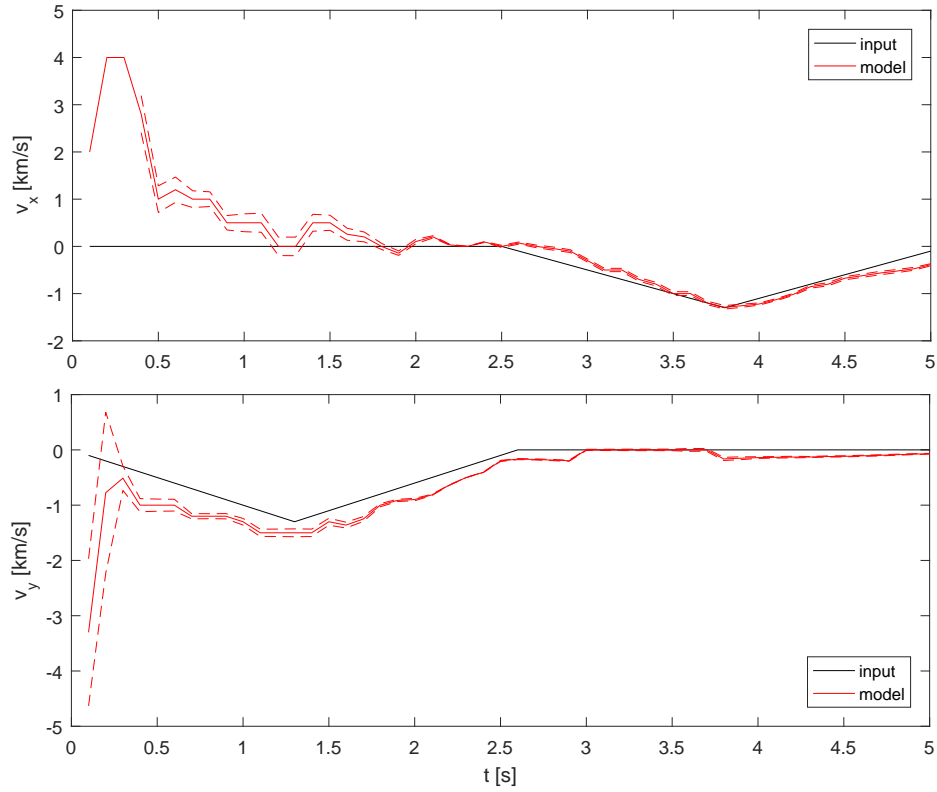


Figure A2. Comparison between input synthetic velocities, labeled with the black line and retrieved velocities from our method, labeled with the red line. Red dotted lines represent standard deviations of estimates. Upper panel depicts the x component of velocity vectors, while bottom panel depicts y component of velocity vectors.